Anal. Chem. **2010,** *82,* 3943–3949

High-Precision Measurement and Analysis of Colloidal Monolayers

Graham Milne, Yongxi Zhao, and Daniel T. Chiu*

University of Washington, Department of Chemistry, Box 351700, Seattle, Washington 98195

This technical note describes an imaging algorithm for analyzing colloidal monolayers, including the measurement of particle-to-particle distances with nanometer-scale resolution and the automated detection of defects and edges, as well as determining the uniformity of the colloid size distribution. The algorithm also allows for the automatic detection and measurement of scaling introduced by nonsquare detector pixels, a common problem in imaging. As an application, we demonstrate the use of this method for spatially calibrating digital video microscopy systems that can be applied in situations where conventional methods may be inappropriate. Here, we provide an overview of the workings of the algorithm, which we have made freely available.

The use of colloidal monolayers and bead-based assays is now ubiquitous in engineering, chemistry, and biology.[1−7] Colloidal monolayers have been used for lithography, where the 2D crystal acts as a lithographic mask for subsequent nanofabrication[3] and for fabricating ordered micro/mesoporous polymer films, which have a wide range of potential applications, from catalysis to cell-culture experiments.[5,6] For these applications in microfabrication, the quality and crystallinity of the colloidal monolayer is important. Besides fabrication, colloidal crystals have also been demonstrated as an ideal stationary phase for chemical separation.[7] Here, again the crystallinity and lack of defects are important in ensuring the performance of the final device. Colloidal crystals with well-defined defects, however, are useful in other applications, such as in photonic crystals and devices where the defects allow for high-efficiency light propagation.[4] Optical sensors have also been developed using colloidal monolayers of gold, where the binding of analytes changes the plasmon resonance of the 2D crystal.[8] The physical attributes of the colloidal crystal are again critical for these applications. In addition to the practical applications of colloidal monolayers described above, they are also subjects of intense fundamental studies in colloid physics.[9]

For all of these applications, it is of high practical value to be able to analyze the various parameters (dislocations, domain boundaries, edges, holes, and colloid-size distributions) of the colloidal crystal in a precise and automated fashion. Here, we describe a method and algorithm for achieving this task.

In addition to being able to quantify the various parameters of a 2D crystal, our algorithm is also capable of determining the bead-to-bead distance with nanometer-scale resolution. This capability may find use for quantifying biological coatings used in bead-based assays. In principle, differences in the bead-to-bead distance before and after the surface-coating reaction reflect changes that occurred at the surface and the thickness of the coated layer. Surface functionalization of microspheres underlies many important biological assays and pharmaceutics, and given the complexity and time-consuming nature of using electron microscopy to visualize the presence of the coating, our approach may offer a convenient initial screen of the success of the surface reaction.

To demonstrate our algorithm, we have chosen a simple application in microscopy. Beads of a known size are often used casually to calibrate distances in the microscope image plane. This method is popular, although not very accurate, owing to difficulties in demarcating the boundary of the bead in an optical image. Nevertheless, the use of this procedure to calibrate microscope images is a common practice because of the ease and simplicity of the method. It is possible to calibrate distances using traditional approaches, such as a stage micrometer, but many situations would benefit from an alternative method. In our own experiments, the spatial constraints placed by the sample chamber on our microscope made it impossible to use a standard stage micrometer scale to calibrate our images. As a result, we have chosen this simple application to illustrate our technique and algorithm. This procedure is simple and robust and is no more complex than what many researchers already do when they pipet beads onto their coverslips to calibrate their images. The key point is that our algorithm offers nanometer-scale resolution, an improvement in measurement accuracy of several orders of magnitude over traditional visual inspection.

EXPERIMENTAL METHODS

Formation of Colloidal Monolayers. For this work, our first task was to produce two-dimensional close-packed colloidal crystals using the simplest method possible. We found that the

* To whom correspondence should be addressed. E-mail: chiu@chem.washington.edu.

(1) Kawaguchi, H. *Prog. Polym. Sci.* **2000**, *25*, 1171–1210.
(2) Hartman, A. W.; Doiron, T. D.; Fu, J. *J. Res. Natl. Inst. Stand. Technol.* **1992**, *97*, 253.
(3) Burmeister, F.; Badowsky, W.; Braun, T.; Wieprich, S.; Boneberg, J.; Leiderer, P. *Appl. Surf. Sci.* **1999**, *144−145*, 461–466.
(4) Stein, A.; Schroden, R. C. *Curr. Opin. Solid State Mater. Sci.* **2001**, *5*, 553–564.
(5) Zhang, T.; Qian, J.; Tuo, X.; Yuan, J.; Wang, X. *Colloids Surf., A* **2009**, *335*, 202–206.
(6) Andersson, A. S.; Glasmastar, K.; Hanarp, P.; Seantier, B.; Sutherland, D. S. *Nanotechnology* **2007**, *18*, 205303.
(7) Zheng, S.; Ross, E.; Legg, M. A.; Wirth, M. J. *J. Am. Chem. Soc.* **2006**, *128*, 9016–9017.
(8) Okamoto, T.; Yamaguchi, I.; Kobayashi, T. *Opt. Lett.* **2000**, *25*, 372–374.
(9) Han, Y.; Shokef, Y.; Alsayed, A. M.; Yunker, P.; Lubensky, T. C.; Yodh, A. G. *Nature* **2008**, *456*, 898–903.

10.1021/ac902722d © 2010 American Chemical Society
Published on Web 03/30/2010

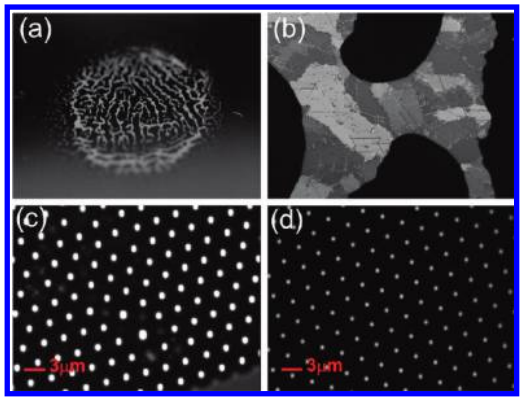

Figure 1. Polymer spheres (3 μm) imaged with a range of magnifications: (a) image of a dried droplet on the coverslip, (b) imaged using a 20× objective with oblique illumination, and (c) imaged with a 100× objective. Note elongation, dislocations, and large particles, along with camera saturation due to improper illumination settings. (d) Imaged with 100× objective with optimum lighting and highly uniform hexagonal close-packing.

retreating water−air interface of an evaporating droplet can generate suitable monolayers, which is in line with previous work,[2,10−13] where the ability of a retreating interface to form close-packed colloidal monolayers has been well studied. We prepared samples of 3 μm-diameter polymer microspheres (Duke Scientific, R0300, lot 28980), suspended in Milli-Q water with a measured concentration of 0.018% solid by mass. Droplets (0.2 mL) were then deposited on conventional microscope coverslips (VWR, no. 1) and allowed to evaporate at normal room temperature and pressure. We chose these microspheres because they are sold as NIST-traceable particle size standards.

Figure 1 shows images of a monolayer produced by evaporating a droplet, at various magnifications, and is typical of the samples used throughout this work. Figure 1a shows the entire evaporated droplet. Figure 1b shows a section imaged with a 20× objective. Oblique illumination was used, which allows clear identification of the colloidal crystal domains, despite the fact that the monolayer is flat. Both parts c and d of Figure 1 were captured with a 100× oil immersion objective. For the purposes of this work, Figure 1c is representative of a "poor" region of the sample, containing an uneven particle size distribution, crystal dislocations, an edge, and inappropriate lighting. Figure 1d is an example of a "good" region, the hexagonal packing is highly uniform and the illumination has been adjusted to enable accurate particle identification.

Calibration of Distance between Microspheres Using TEM. The colloidal samples we used came prepared in a solution containing surfactants to prevent aggregation of the microspheres in suspension. Since our goal is to develop a quick and simple method for calibrating a microscope, we chose not to wash our solutions prior to evaporation of the solution and formation of the colloidal monolayer. To determine the typical center-to-center spacing between adjacent spheres and to ensure the bead-to-bead distance was unaffected by the presence of surfactants during drying,[14,15] we opted to analyze our samples using a transmission electron microscope (TEM) (FEI Tecnai G2 F20). This microscope is calibrated regularly using both gold and silicon crystal samples, which sets the TEM resolution at 0.11 nm. Figure 2 shows a typical image from our TEM experiments.

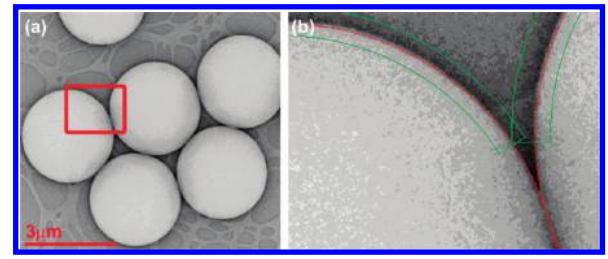

Figure 2. (a) TEM image of our 3 μm polymer spheres, showing hexagonal close-packing under normal drying conditions. (b) By analyzing the circular edges of the particles, we estimate the maximum interparticle separation to be of the order of only 1−2 pixels or 4−8 nm. This approach is necessary due to blurring of the TEM image around the intersphere boundary region. We also note the spheres in our samples are highly uniform in size. The colored lines in the image are produced by the algorithm we developed for measuring the circular edge. The red curve represents the estimated particle edge.

It has been noted that the intense electron bombardment associated with a TEM can chemically weaken and ultimately melt polymer micrsopheres.[16,17] By only using images obtained at the very beginning of the TEM session, we were able to minimize the impact of electron absorption, allowing us to produce accurate measurements of the polymer sphere size. Previous reports have also noted that removing polymer microspheres from suspension through drying can cause them to shrink.[14,16] The spheres we used were hard-dyed, with dye incorporated throughout the polymer matrix. These hard spheres are not expected to shrink significantly upon drying. Thus, the TEM images enable us to size spheres accurately.

Careful analysis of the images obtained from our TEM experiments suggests our samples were highly monodisperse, with measured diameters in the range 3 ± 0.1 μm (Figure 2a), which is in excellent agreement with the manufacturer's specifications. Additionally, we measured the maximum interparticle separation to be at most 4−8 nm (Figure 2b). Therefore, the above-mentioned potential issues did not adversely affect the formation of a uniform monolayer of microshperes.

Algorithm and Software. The most critical component of the method presented here is the computational algorithm that is used to assess the image of the two-dimensional colloidal monolayer. Our custom software was implemented in the LabVIEW development environment, which is now ubiquitous in laboratories around the world. The source code used for the work presented in the technical note is freely available for download from our Web site.[18] In the next section we discuss, in sequence, the key stages of our algorithm.

(10) Denkov, N. D.; Velev, O. D.; Kraichevsky, P. A.; Ivanov, I. B.; Yoshimura, H.; Nagayama, K. *Nature* **1993**, *361*, 26.
(11) Velev, O. D.; Lenhoff, A. M. *Curr. Opin. Colloid Interface Sci.* **2000**, *5*, 56–63.
(12) Vanmaekelbergh, D.; Liljeroth, P. *Chem. Soc. Rev.* **2005**, *34*, 299–312.
(13) Zhou, Z.; Li, Q.; Zhao, X. S. *Langmuir* **2006**, *22*, 3692–3697.
(14) Dobashi, T.; Yeh, F.; Ying, Q.; Ichikawa, K.; Chu, B. *Langmuir* **1995**, *11*, 4278–4282.
(15) Koh, Y. K.; Yip, C. H.; Chiang, Y.; Wong, C. C. *Langmuir* **2008**, *24*, 5245–5248.
(16) Megens, M.; van Kats, C. M.; Bsecke, P. *Langmuir* **1997**, *13*, 6120–6129.
(17) Davis, S. Electron Microscopy. In *Colloid Science: Principles, Methods and Applications*; Cosgrove, T., Ed.; Blackwell Publishing: Ames, IA, 2005; pp 266−282.
(18) Milne, G. http://faculty.washington.edu/gmilne/colloidal_calibrator.htm.

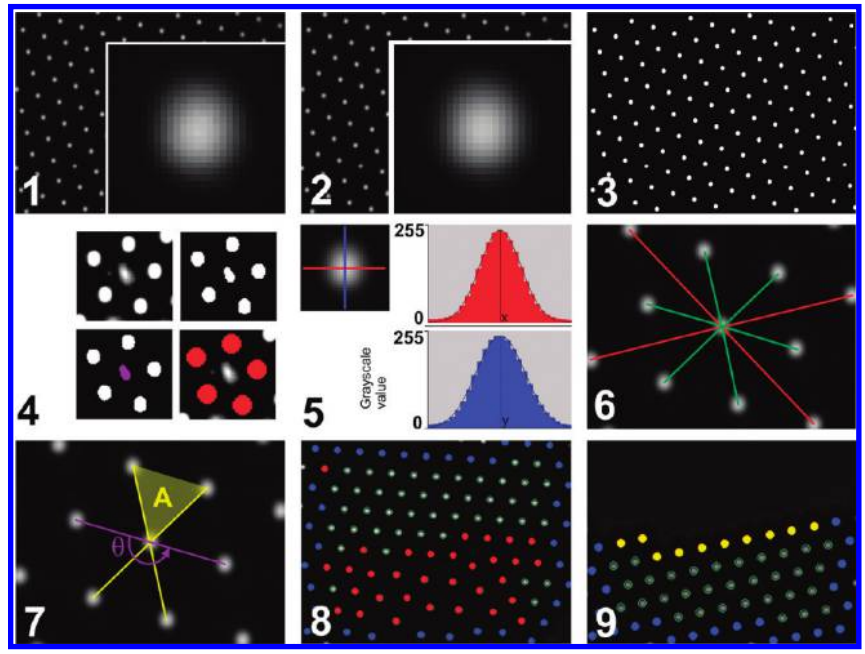

Figure 3. Collage showing the first nine stages of our algorithm: (1) load an image; inset, "noisy" particle; (2) image preprocessing, including smoothing and noise removal; inset, "smoothed" particle; (3) image binarization and calculation of particle center-of-mass; (4) removal of false matches; (5) subpixel refinement of particle center; (6) determination of six nearest neighbors; (7) analysis of robustness of particle; (8) identification of defects; and (9) identification of edges of the monolayer.

RESULTS AND DISCUSSION

Overview of Algorithm. Figure 3 illustrates the first nine stages of our algorithm. These steps are necessary because there is no guarantee that the area of the colloidal monolayer under examination is free of defects. A number of defects can arise during the formation of colloidal monolayers. These are examined individually in more detail below. Since the spatial calibration of the image is calculated from particles that are embedded in an ordered close-packed hexagonal crystal phase, the automatic detection of defects is a critical component of the algorithm.

Stage 1: Load an Image. This can be a saved bitmap file, a frame from a recorded movie (e.g., avi format) or a live grab from an attached video camera.

Stage 2: Image Preprocessing. Under certain circumstances, enhanced performance may be obtained by applying filters to the image to reduce the impact of factors such as uneven illumination and noise. These functions are supported. If the particle centers appear in the image as dark spots, rather than the bright spots shown in Figure 3 (which is possible in certain optical arrangements), then at this stage the image can be inverted. Because the image is static, a sequence of images recorded at different times can be averaged to reduce the impact of camera noise, which is important for the accurate location of particle centers.

Stage 3: Particle Detection. For this work, we use a blob-analysis approach (also known as thresholding); however, other object detection algorithms could be employed. The illumination is set so that the particle cores appear as bright spots in the image. A threshold intensity level is set, and the image is binarized, resulting in an array of well-defined spots. The 2D center-of-mass of these spots is then used as a first estimate of the particle location.

Stage 4: Remove Suspect Candidates. It is useful to filter the resulting binary image to remove suspect particles (e.g., due to unclean optics) or particles that lie across the border of the image. Particles are assessed on their brightness, size, and circularity relative to the mean values. In Figure 3 (part 4) the interstitial region between disordered particles has registered as a particle but has been identified as a false positive through failing a circularity test.

Stage 5: Refine Particle Center-of-Mass. Using standard particle tracking algorithms, it is possible to refine the center-of-mass of a typical particle to within an accuracy of 0.1 pixel. The primary method is based on the classic particle identification work of Crocker and Grier[19] and involves calculating the brightness-weighted centroid of the region around the candidate particle coordinates; however, other well-known particle tracking techniques, such as template matching, can also be employed.

Stage 6: Identify Each Particle's Six Nearest-Neighbors. This stage is achieved by taking each particle and calculating the Euclidean distance to every other particle in the image, keeping the six shortest results. This stage is similar to the analysis presented by Kumnorkaew et al.[20]

Stage 7: Calculation of Metrics for Identification of Hexagonal Packing. The Euclidean interparticle distances alone cannot be used to reliably detect a crystalline phase because the values are not invariant to rescaling; for example, due to nonunitary pixel aspect ratios (discussed in more detail below). However, with additional metrics this problem can be overcome. This part of the algorithm calculates the areas A of the six triangles formed by the lines joining a particle and its six neighbors along with the angle θ formed where opposing interparticle lines intersect, as shown in Figure 3 (part 7).

Stage 8: Determination of Particles in Crystalline Phase. It is possible to identify robust particles by examining and thresholding the above metrics for each particle, embedded in the hexagonal

(19) Crocker, J. C.; Grier, D. G. *J. Colloid Interface Sci.* **1996**, *179*, 298.
(20) Kumnorkaew, P.; Ee, Y.; Tansu, N.; Gilchrist, J. F. *Langmuir* **2008**, *24*, 12150–12157.

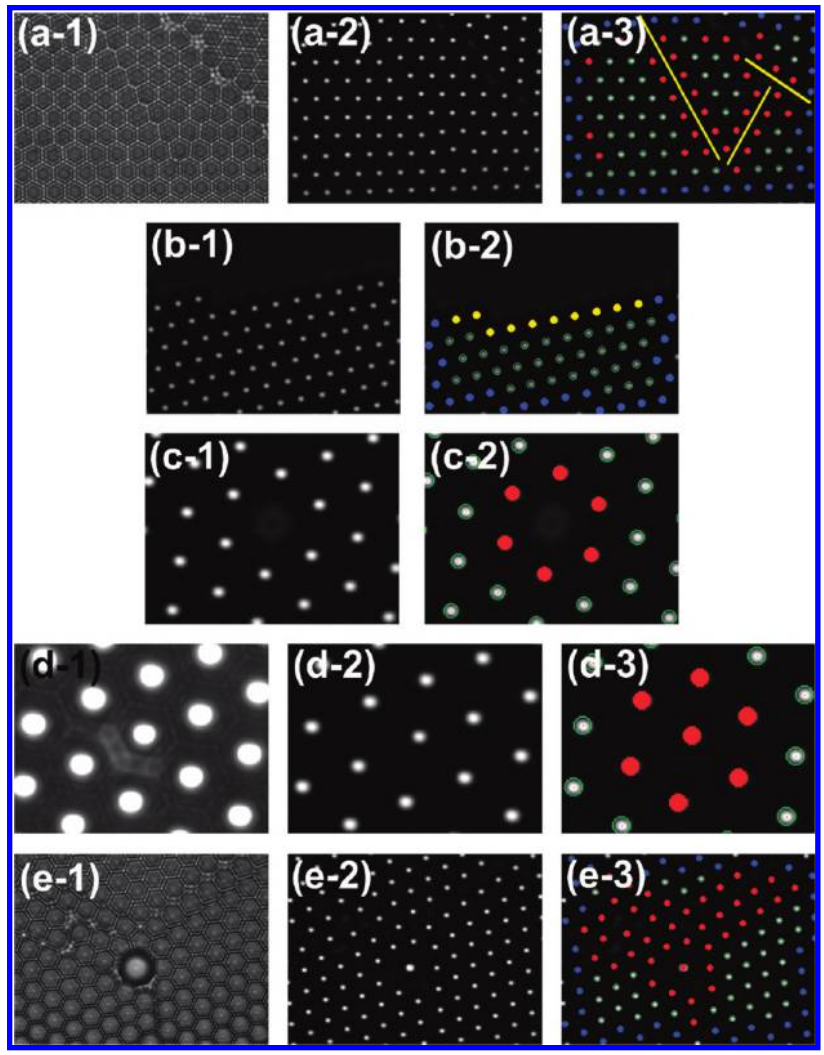

Figure 4. (a-1) Typical image with three dislocations of varying severity; (a-2) same view with optimal illumination conditions; (a-3) automatic identification of significant dislocations; (b-1) image of colloidal monolayer edge; (b-2) automatic detection of the monolayer edge (yellow); (c-1) close-up of a hole in the original image; (c-2) identification of hole; (d-1) close-up of an offset, small particle (center of the image) with increased illumination to highlight size discrepancy; (d-2) same particle using optimal illumination; (d-3) detection of the small particle and the localized disruption to monolayer; (e-1) large particle embedded in a colloidal monolayer; (e-2) same sample, with optimum illumination; (e-3) output from program, showing identification of the disruption caused by the large particle.

crystal structure, which should have six triangles of comparable area A and three pairs of interparticle vectors that are equal in magnitude but opposite in direction ($\theta \approx \pi$). Particles that do not fit this criterion are marked by a red spot and can generally be categorized as either mis-sized, isolated, or adjacent to a dislocation or domain boundary, as shown in Figure 4. Particles that are determined to be embedded in the crystal are termed robust and are outlined with a green circle.

Stage 9: Edge Identification. It is important to isolate particles that are located at the edge of the monolayer. Baumgartl et al.[21] have reported that the accuracy of video-based particle tracking is significantly influenced by the proximity of neighboring particles. As such, particles on the edge of the crystal structure can yield center-of-mass locations that are perturbed slightly relative to those of the embedded, robust particles.

Stage 10: Calculation of Aspect Ratio of Pixels. The hexagonal close-packed structure can be associated with a mesh of equilateral triangles. If the camera pixels are rectangular, this will result in a characteristic uniaxial scaling of the image. The algorithm for recovering the scaling factor is discussed in more detail later.

Stage 11: Determination of Calibration Factors. With the uniaxial scaling factor Ω established, and knowledge of the mean calibrated sphere diameter, the program can then calculate and return real-world calibration factors for the image.

Comparison with a Stage Micrometer. In video microscopy, it is standard practice to spatially calibrate images through the use of a stage micrometer. High-resolution stage micrometers are commercially available and are generally straightforward to use; however, the method does carry some limitations. First, many stage micrometers contain rulings along a single axis, making simultaneous, orthogonal calibration of the two axes of the image plane difficult. Second, calibration using this approach requires human analysis of the acquired image, introducing a possible source of error. Finally, stage micrometers are typically designed for use in standard microscope setups and are not necessarily suited to situations where there are restrictions on the acceptable form factor of the object under scrutiny. As an example, in our

(21) Baumgartl, J.; Bechinger, C. *Europhys. Lett.* **2005**, *71*, 487–493.

laboratory, our microscope is fitted with a three-axis piezo microstage (Nano-PDQ350, MadCity Laboratories), the central sample aperture of which is too small to accommodate standard stage micrometers.

Using an equivalent optical system, we compared our method with a conventional stage micrometer (NT30-593, Edmund Optics), imaged through an infinity-corrected 100× objective and recorded with a CCD camera with square pixels (Prosilica GC660M). To calibrate the image, we took a line profile horizontally through the image of the stage micrometer, from which we manually measured the real-world calibration factor to be 18.35 ± 0.1 pixels per micrometer.

Running our algorithm on Figure 1d results in a measured calibration factor of 18.17 ± 0.11 pixels per micrometer, which is in agreement with the manual line-profile measurement. In this case, the standard deviation produced by our algorithm is derived from the standard deviation of the mean robust interparticle separation distance.

Additional Observations on Performance of Algorithm. Our program produces a variety of statistical indicators, allowing the user to clearly monitor the performance and accuracy of the measurement process. As long as the illumination and focus is adjusted to prevent saturation, which results in a clear, well-defined profile for each individual particle, as in Figure 1d, we have found that the results produced by the algorithm are insensitive to small (micrometer) movements in the vertical axis (this can happen, for example, due to mechanical drift of the microscope stage).

Particles close to the edges of the image must be considered separately, due to the fact that some of their neighbors are likely to be out of the field of view. This can lead to difficulties in judging whether or not these particles are robust and reside embedded in a hexagonal lattice. These particles are automatically identified through the observation that the orthogonal distance between their measured center-of-mass and the nearest image boundary is less than the mean particle−neighbor separation distance. It is possible to include them in analysis based on their relationship to neighboring particles that do reside in the field of view. This is included as a user option but can potentially be a source of error.

Dislocations and Domain Boundaries. During the formation of the monolayer, nucleation can occur simultaneously at multiple sites within the droplet,[10] which leads to the formation of distinct crystal domains in the monolayer (clearly visible in Figure 1b). The presence of dislocations or domain boundaries in the image leads to a characteristic distribution of nonrobust particles, making their identification straightforward. Figure 4(a-3) shows three detected dislocations of varying severity.

Colloidal crystal dislocations and their applications are still an area of active study.[22,23] Researchers have recently demonstrated, for example, that dislocations in a colloidal crystal can be used as optical phase modulators to create optical vortices.[24,25] For such applications, we envisage that our freely available software could be of use to researchers who would like to automate the detection of dislocations in colloidal crystals.

(22) Lipowsky, P.; Bowick, M. J.; Meinke, J. H.; Nelson, D. R.; Bausch, A. R. *Nat. Mater.* **2005**, *4*, 407–411.
(23) Ling, X. S. *Nat. Mater.* **2005**, *4*, 360–361.
(24) MacDonald, M. P.; Prentice, P.; Dholakia, K. *New J. Phys.* **2006**, *8*, 257.
(25) MacDonald, M. P.; Dholakia, K. *Phys. C* **2008**, *468* (7−10), 508–513.

Detection of Colloidal Monolayer Edges. The detection of the edges of the colloidal monolayer, distinct from crystal boundary domains or dislocations, is a potentially useful capability, enabling, as an example, automatic scanning of the sample. Superficially, from the point of view of our algorithm, there is no difference between particles adjacent to a dislocation or domain edge (e.g., Figure 4(a-1)) and particles lying at the edge of the monolayer. This is due to the fact that in both cases the six nearest neighbors for these particles do not lie in an equidistant hexagonal arrangement and therefore fail to meet the criterion for a robust particle.

To identify an edge in the monolayer, an additional step must be introduced where failed, nonrobust particles are re-examined. Figure 4(b-1) shows an image of a well-defined edge from our test experiments, which can be determined by analyzing the nearest-neighbor distances. Whereas robust particles embedded in the monolayer have six approximately equidistant neighbors separated by a distance L, particles on a well-defined monolayer edge will have, as shown in Figure 4(b-2), nearest neighbors separated by distances approximating values of nL', $\sqrt{3}L'$ or $\sqrt{7}L'$, where n is an integer and $L' = cL$. Here, c is a small correction factor due to the effects described in Baumgartl et al.[21] If the monolayer edge is not well-defined, the program can estimate the edge based on an analysis of the local particle density.

Holes. During the formation of the monolayer, it is possible for holes to form in the hexagonal lattice, as shown in Figure 4c. The presence of a singular hole does not significantly perturb the surrounding lattice. The characteristic spatial distribution of particles associated with a hole is therefore straightforward to identify, which our program does automatically.

It is possible for larger holes to form, which in the monolayer may involve more than one adjacent lattice site. Such structures can be identified as special cases of a monolayer edge. Holes are only easy to identify when the surrounding structure is a uniform hexagonal lattice.

Small Particles. Particles that are smaller than the general bulk can be incorporated into the monolayer. The presence of the small particle does not appear to considerably perturb the overall structure of the surrounding hexagonal lattice. In our tests, we found that smaller particles generally tend to sit slightly offset from the center in the lattice site that they occupy, a displacement that is quantifiable. Because of this consistent behavior, our program can automatically identify the presence of small particles (Figure 4d). An approximate size for the smaller particle can be measured; however, a small error is inevitably introduced due to the slight variation in the height of the smaller particle compared with the average height of the surrounding particles.

Large Particles. The effect of larger particles on the surrounding matrix contrasts markedly with the small-particle case. Large particles can cause considerable disruption to the uniformity of the surrounding monolayer, introducing voids and dislocations, as shown in Figure 4e. Again, the program can detect the presence of an oversized particle; however, in this case size estimation is not possible due to the unpredictable distribution of nearest neighbors.

Rectangular Pixel Correction. One of the key advantages of this method of image calibration is that the geometry of the close-packed hexagonal 2D crystal can be used to detect and

recover the relative scaling of the two principle axes of the image. As an example, lateral distortion of the image can occur because some camera sensors have rectangular pixels, whereas computer pixels are typically square.

Figure 5(a-1) shows a close-up of Figure 1d after it has been resampled to shrink its width to 80% of the original value. The particles in the image, which in reality form the vertices of equilateral triangles, appear to form the vertices of a scalene triangle due to the horizontal scaling. Figure 5(a-2) illustrates the quantities of interest when analyzing the triangular arrangement of the particles under scrutiny. Finally, Figure 5(a-3) shows the original image for comparison, with three particles forming the vertices of an equilateral triangle.

From Figure 5(a-2) and using Pythagoras' Theorem, we note the following two relationships:

$$\alpha_x^2 + \alpha_y^2 = L^2 \tag{1}$$

$$\beta_x^2 + \beta_y^2 = L^2 \tag{2}$$

These can then be equated and trivially rearranged to give

$$\alpha_x^2 - \beta_x^2 = \beta_y^2 - \alpha_y^2 \tag{3}$$

We note that in Figure 5a, the images are related by a scaling factor along the horizontal (x) axis, which we will define as Ω_x. The coordinates of the vertices of the two triangles in Figure 5(a-2) can be mapped through the relationships

$$\begin{aligned} \alpha_x &= \Omega_x a_x \\ \alpha_y &= a_y \\ \beta_x &= \Omega_x b_x \\ \beta_y &= b_y \end{aligned} \tag{4}$$

By substituting these values into eq 3 and rearranging, we get

$$1 = \frac{b_y^2 - a_y^2}{\Omega_x^2 a_x^2 - \Omega_x^2 b_x^2} \tag{5}$$

which then leads to an expression for the scaling factor Ω_x:

$$\Omega_x = \left| \left(\frac{b_y^2 - a_y^2}{a_x^2 - b_x^2} \right) \right|^{1/2} \tag{6}$$

Taking the absolute value in eq 6 removes the dependence on which particle in a given triangle is chosen as the origin of the local coordinate system.

For the case where the compression has occurred along the y-axis (e.g., if the image has been rotated 90°), the analysis is similar, with

$$\begin{aligned} \alpha_x &= a_x \\ \alpha_y &= \Omega_y a_y \\ \beta_x &= b_x \\ \beta_y &= \Omega_y b_y \end{aligned} \tag{7}$$

which ultimately leads to the expression

$$\frac{1}{\Omega_y} = \left| \left(\frac{b_y^2 - a_y^2}{a_x^2 - b_x^2} \right) \right|^{1/2} \tag{8}$$

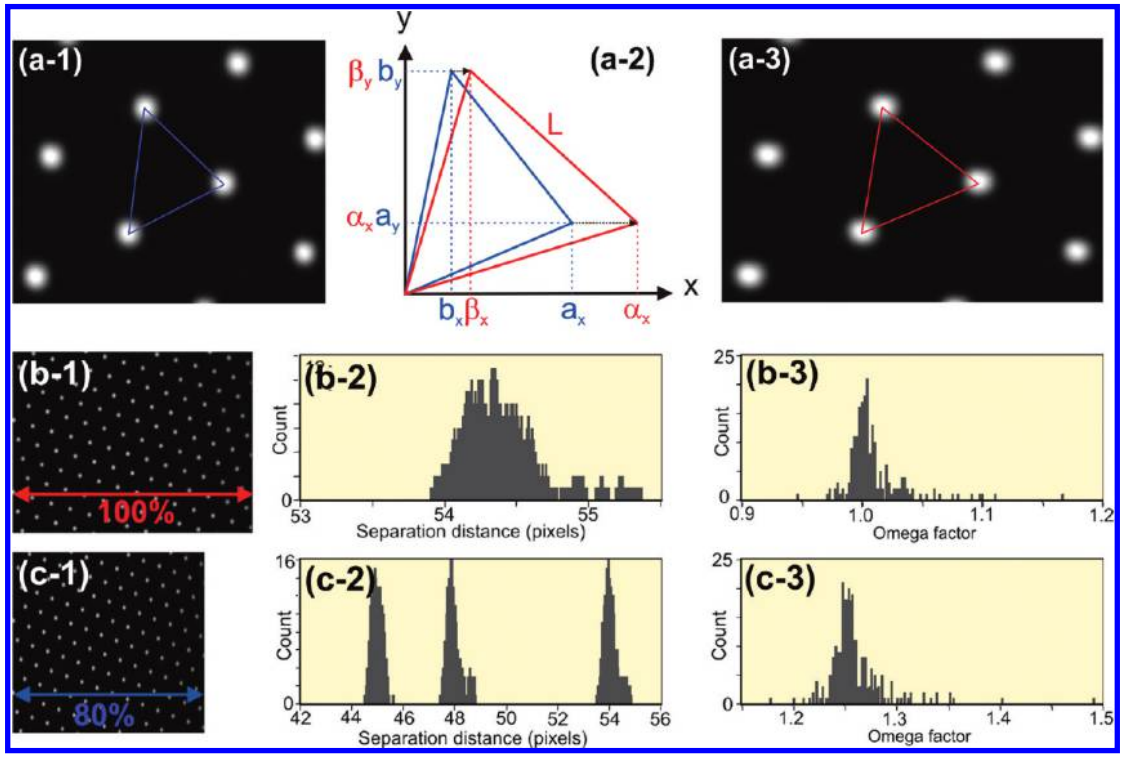

Figure 5. (a-1) Image after 80% horizontal scaling; adjacent particles form vertices of scalene triangles; (a-2) illustration of significant factors for calculating scaling factor; (a-3) restoration of true image showing characteristic triangle; (b-1) original, unscaled image; (b-2) histogram of measured nearest neighbor distances of robust particles; (b-3) histogram of measured Ω scaling factors; (c-1) image scaled to 80% of original width; (c-2) distribution of measured nearest neighbor distances for resampled image; and (c-3) measured Ω factors for resampled image.

We can define a universal factor, Ω, with the interpretation that a value greater than 1 corresponds to a horizontal contraction (Ω_x), while a value less than 1 corresponds to a vertical image contraction (Ω_y).

Figure 5(b) shows a typical statistical output from a test image (Figure 1d). Figure 5(b-2) shows the distribution of nearest-neighbor distances, in pixels, while Figure 5(b-3) shows the corresponding distribution of calculated Ω factors. Note that for the unscaled image, the Ω-factor distribution is peaked tightly around a value of 1.

Figure 5(c-2) shows the nearest neighbor distributions for the resampled image. Note that the scaling means that there are now three different principle nearest neighbor distances, reflecting the three sides of the scalene triangle. Analysis of the Ω factors associated with each scalene triangle in the resized image results in a Ω factor distribution centered on a value of 1.25 (Figure 5(c-3)), which corresponds to our choice of 80%.

CONCLUSIONS

In this technical note, we described a technique and algorithm for the automated analysis of colloidal monolayers, which we believe will have wide practical utility for applications ranging from microfabrication to the development of photonic devices and optical sensors. This algorithm is capable of characterizing many important features of the colloidal crystal, including dislocations, domain boundaries, edges, holes, distribution in particle size, and bead-to-bead distances, all performed with high accuracy and in a rapid automated fashion.

Additionally, because of the extreme simplicity and high resolution of this technique for extracting bead-to-bead distances, we believe it may also find use as a simple and rapid check for determining the presence and thickness of proteins or DNA coated onto beads. Surface functionalization of microspheres is widespread, and this technique may serve as a rapid initial screen of the success of the functionalization reaction as it requires only a simple optical microscope and just minutes to determine the change in bead-to-bead distance prior to and after the desired surface reaction.

To illustrate our algorithm, we chose to address a practical issue we faced in our own laboratory for calibrating microscope images. For this application, the procedure is extremely simple, involving only the pipetting of a small volume of bead solution onto the coverslip and letting it dry. Here, we deliberately used commercially available microspheres, with no efforts to wash the samples or to control the size distribution beyond what is provided by the vendor. This ability to calibrate microscope images easily and with high precision is particular timely, given recent rapid advances in super-resolution optical microscopy.

ACKNOWLEDGMENT

Y.Z. acknowledges a fellowship from the China Scholarship Council. We are grateful to NIH (Grant GM 085485) for the support of this work.

Received for review November 30, 2009. Accepted March 15, 2010.

AC902722D